



Measuring the Metallicity of Early-type Galaxies

Yu-Zhong Wu

Key Laboratory of Optical Astronomy, National Astronomical Observatories, Chinese Academy of Sciences, Beijing 100101, People's Republic of China

Received 2019 November 24; revised 2020 January 27; accepted 2020 February 10; published 2020 April 20

Abstract

We use data for 6048 early-type galaxies (ETGs) from Galaxy Zoo 1 that have been cross-matched with the catalog of the MPA-JHU emission-line measurements for the Sloan Digital Sky Survey Data Release 7. We measure the metallicity of these ETGs by excluding various ionization sources, and study other properties as well. We use the optimal division line of $W2-W3 = 2.5$ as a diagnostic tool, and for the first time derive metallicity measurements for 2218 ETGs. We find that these ETGs actually are closer to H II regions as defined by Kauffmann et al. in the Baldwin–Philips–Terevich diagram, and they display younger stellar populations. We present a full mass–metallicity relation and find that most ETGs have lower metallicities than star-forming galaxies (SFGs) at a given galaxy stellar mass. We use five metallicity calibrators to check our results. We find that these metallicity indicators (R23, O32, and O3S2) give consistent results. We suggest that the remaining two metallicity calibrators, which increase metallicity by N-enrichment, can be used to calibrate metallicities for SFGs, but not to estimate the metallicities of ETGs.

Unified Astronomy Thesaurus concepts: [Galaxy abundances \(574\)](#); [Galaxy evolution \(594\)](#); [Galaxy accretion \(575\)](#)

1. Introduction

Early-type galaxies (ETGs) generally appear as red, passive/retired objects, almost without gas and dust. Lenticular and elliptical galaxies are ETGs; recent studies have demonstrated that ETGs usually contain a multiphase interstellar medium (ISM; Herpich et al. 2018) comprising neutral hydrogen (e.g., Krumm & Salpeter 1979; Goudfrooij et al. 1994; Oosterloo et al. 2010; Serra et al. 2012; Lagos et al. 2014; Woods & Gilfanov 2014), molecular gas (Combes et al. 2007; Davis et al. 2015), halos of hot gas (Sarzi et al. 2013), and dust (Goudfrooij & de Jong 1995). Gas in the ISM of ETGs tends to be accompanied by low-efficiency star formation (SF).

Mounting evidence reveals recent or ongoing SF in some ETGs. Yi et al. (2005) demonstrated that recent SF activity could be identified in approximately 15% of their sample of 160 ETGs. Using a sample of roughly 2100 Sloan Digital Sky Survey (SDSS) ETGs, Kaviraj et al. (2007) have shown that $\sim 30\%$ of their sample experience low-level SF, deriving $\sim 1\%$ – 3% of the total galaxy stellar mass. This implies that low-level SF is common in ETGs.

Much attention has been focused on explaining SF in ETGs. One possible cause is gas accretion introduced by minor mergers (Kaviraj et al. 2009; Thilker et al. 2010). Geréb et al. (2016) posited that an extended (~ 60 kpc) stellar stream provides direct evidence for gas accretion, showing that a merger event in GASS 3505 happened in the recent past. Another possible cause of SF is accretion from the intergalactic medium (IGM). With regard to the formation of Hoag's Object, Finkelman et al. (2011) suggested that the core and H I disks of Hoag's Object were formed at different evolutionary phases, and that the forming of the disks was prolonged by “cold” accretion of pristine gas from the IGM.

Gas-phase metallicity is crucial for studying various aspects of the evolution of galaxies. Several attempts to obtain

metallicity calibrations for H II regions of ETGs have been made. Zhang et al. (2017) studied the impact of the diffuse ionized gas (DIG) on metallicity measurements at kiloparsec scales with the data from Mapping Nearby Galaxies at APO survey. Kumari et al. (2019) estimated the effect of DIG contamination on metallicity measurements, and obtained metallicity calibrators for the DIG and low-ionization emission region.

To date, metallicity measurements of ETGs have only been provided by Athey & Bregman (2009), Annibali et al. (2010), Bresolin (2013), and Griffith et al. (2019); they have obtained dozens of oxygen abundances from optical emission lines. Here, we investigate the metallicity of ETGs with a large sample, and study the properties of these ETGs. In Section 2, we provide a brief description of the ETG sample and our data. Excluding several ionization sources, we derive the metallicity of ETGs and explore the properties of these ETGs in Section 3. Finally, our results are summarized in Section 4.

2. The Data

In this work, we utilize the data of the SDSS Seventh Data Release (DR7; Abazajian et al. 2009). The SDSS DR7 provides the spectra of more than one billion galaxies, covering a wavelength range from 3600 to 9200 Å, with mean spectral resolution $R \sim 1800$ and assembled from 3" diameter fibers. The measurements of stellar masses, emission-line fluxes, and star formation rates (SFRs) can be obtained from the SDSS DR7 catalog of the Max Planck Institute for Astrophysics–John Hopkins University (MPA–JHU), which is publicly available;¹ this catalog supplies the spectra measurements of about 900,000 galaxies.

First, we choose galaxies at $0.04 < z < 0.12$ to avoid the bias of mass–metallicity (MZ) relations from the aperture (Kewley et al. 2005). The aperture-covering fractions are required to be $>20\%$ for all galaxies, and the parameters are computed from the r -band Petrosian and fiber magnitudes.

 Original content from this work may be used under the terms of the [Creative Commons Attribution 4.0 licence](#). Any further distribution of this work must maintain attribution to the author(s) and the title of the work, journal citation and DOI.

¹ <https://wwwmpa.mpa-garching.mpg.de/SDSS/DR7/>

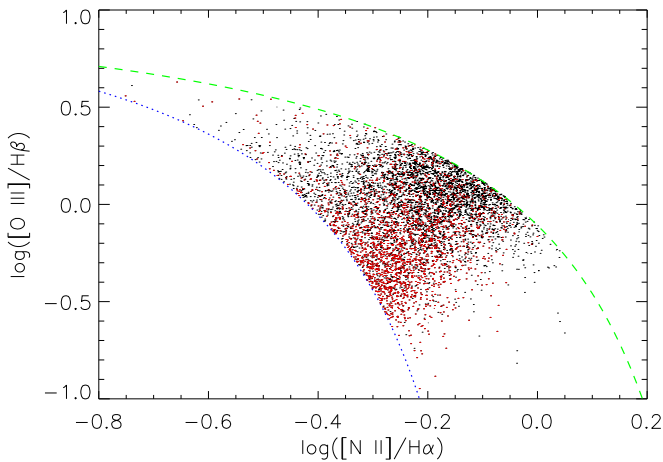


Figure 1. BPT diagnostic diagram. The black and red dots show initial composite ETGs selected; the red dots are final ETGs with metallicity measurements. The dotted blue curve represents the Kauffmann et al. (2003) semi-empirical lower limit for SFGs; the green dashed curve on this diagram is the theoretical “extreme starburst line” obtained by Kewley et al. (2001) as an upper boundary for SFGs.

For our sample we select galaxies with a signal-to-noise ratio (S/N) > 3 for $H\alpha$ and $H\beta$, and with $S/N > 2$ for $[O\ II]\lambda\lambda\ 3227, 3229$, and $[N\ II]\lambda 6584$. Moreover, because the SFR FLAG keyword represents the measuring status of SFRs in the catalog, the keyword must be zero. As a result, we have an initial sample of 140,589 galaxies.

We first take the galaxies with $n_{\text{Sersic}} > 2.5$ to be ETGs, and then base our galaxy morphologies on Galaxy Zoo 1 (Lintott et al. 2008, 2011) to match our sample with that found in Table 2 of Lintott et al. (2011). The Sérsic index comes from the New York University Value-Added Galaxy Catalog² (NYU-VAGC; Blanton et al. 2005). We cross-match the NYU-VAGC with our initial sample within $2''$, and obtain 133,101 galaxies. Then we choose the galaxies with $n_{\text{Sersic}} > 2.5$, showing a sample of 42,916 galaxies. Next, we utilize Galaxy Zoo 1 to select those galaxies with an elliptical probability that is higher than 0.5 (Herpich et al. 2018), and match them with those found in Table 2 of Lintott et al. (2011). This produces a sample of 16,623 ETGs.

We also need to assess the star-forming properties of our ETG sample and the probability of their contribution of an active galactic nucleus (AGN) on the Baldwin–Philips–Terevich (BPT) diagram (Baldwin et al. 1981). Based on several models, Kewley et al. (2001) and Kewley et al. (2006) constructed extreme starburst lines, which are an upper limit on the emission-line strengths in star-forming galaxies (SFGs). Galaxies that lie below the two curves are dominated by star formation (Griffith et al. 2019). Therefore, we consider only those galaxies that are located in the composite region on the BPT diagram in this work, which means that our sample contains 6048 composite ETGs (see the BPT diagram in Figure 1).

To further study the properties of ETGs, we utilize the *Wide-field Infrared Survey Explorer* (Wright et al. 2010) catalog to explore their properties. This survey provides coverage of the whole sky in four bands: $W1$, $W2$, $W3$, and $W4$, with the central wavelengths of 3.4, 4.6, 12, and 22 μm . The accurate position, four-band fluxes, four-band instrumental profile-fit photometry

magnitudes, and their instrumental profile-fit photometry S/N ratios are publicly available.³ We cross-match the ETG sample using the ALLWISE source catalog within $2''$ and $S/N > 3$ for $W2$ and $W3$, and obtain 4177 galaxy sample.

In the MPA-JHU catalog for the SDSS DR7, M_* and SFR measurements assumed a Kroupa (2001) initial mass function (IMF) and are corrected by a Chabrier (2003) IMF. In SFGs, gas-phase oxygen abundances are estimated by using the abundance measurements of extragalactic H II. Because ETGs include many other ionization sources, such as AGN activities, cosmic rays, shocks, and old, hot stars, Griffith et al. (2019) obtained the metallicities of three ETGs by considering the influence of these ionization sources on the abundance measurements. In addition, Brown et al. (2016) used a sample of about 200,000 SFGs to estimate the performance of some abundance indicators, and suggested that the O3N2 method of Pettini & Pagel (2004) is the most perfect calibrator. In the higher stellar masses, the MZ relation calibrated by the PP04-O3N2 indicator can display a consistency with the direct method (T_e method) MZ relation (Andrews & Martini 2013). In addition, the O3N2 indicator adopts flux ratios of more neighboring lines than other indicators, avoiding more substantial effects of atmospheric dispersion (Griffith et al. 2019). In this Letter, we utilize PP04-O3N2 as our abundance estimator.

In addition to the metallicity calibrator of PP04-O3N2, in this Letter we also use another five metallicity calibrators to calculate oxygen abundance of ETGs: Tremonti et al. 2004 (T04), Jones et al. (2015, Jon15), Curti et al. (2017, Curti17), Sánchez-Almeida et al. (2018, Sánchez18), and Sanders et al. (2018, Sander18).

3. Results

3.1. The Metallicity Measurement of ETGs

The gas-phase oxygen abundance of the warm ISM can be estimated by metallicity measurements of extragalactic H II regions and photoionization models. In ETGs, many ionization sources, such as AGN activities, shocks, post-asymptotic giant branch (PAGB) stars, and cosmic rays. In this work, the AGN activities can be excluded due to the fact that our sample consists of composite ETGs, dominated by SF (Griffith et al. 2019), and we do not need to consider the AGN photoionization. Regarding the shock excitation mechanism, the observed line fluxes can be influenced by shocks. Compared with the typical densities and velocities suggested by Sparks et al. (1989), the shock energy is too low by two orders of magnitude (Athey & Bregman 2009). In Griffith et al. (2019), we can see that $[N\ II]/H\alpha$ ratio excited by the shock from a Small Magellanic Cloud-like galaxy (Allen et al. 2008) is far lower (about one order of magnitude) than the ratio of galaxies lying in composite or AGN regions. From Figure 4 of Griffith et al. (2019), we can also see that the line flux ratio excited by the cosmic ray or extra heat is far lower than that excited by galaxies located in composite or AGN region on the BPT diagram, and excludes the two ionization sources. In addition, because PAGB stars adopting the excitation source can provide energy on the same order of magnitude as weak AGNs, Belfiore et al. (2016) suggested that many galaxies,

² <http://sdss.physics.nyu.edu/vagc-dr7/vagc2/sersic/>

³ <https://irsa.ipac.caltech.edu/cgi-bin/Gator/nph-dd>

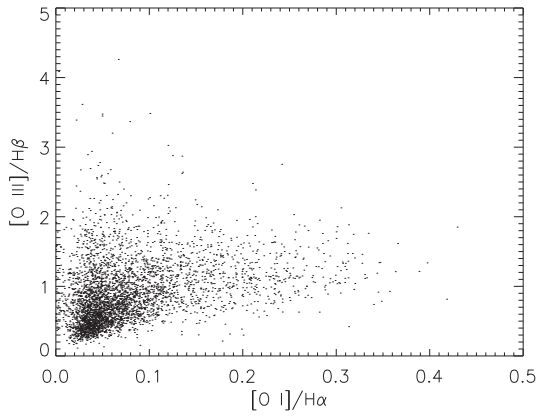


Figure 2. Diagnostic diagram of $[O\text{ I}]/H\alpha$ and $[O\text{ III}]/H\beta$, which identifies ionization from the stellar population with the SD progenitor contribution proposed by Woods & Gilfanov (2014). Galaxies with $[O\text{ I}]/H\alpha > 0.5$ are dominated by SD ionization, and exist outside of the plot.

dominated by SF, are misclassified as active ones (Griffith et al. 2019).

Because the probability of the $[\text{Ne III}]\lambda 3869$ photoionization transition is far lower than one of the collisional cross-section, Athey & Bregman (2009) suggested that the line is an important index of collisional excitation; they excluded NGC 4125 and NGC 2768 from their sample due to the fact that they have clear $[\text{Ne III}]\lambda 3869$ fluxes. This demonstrates that the two objects have more a complicated excitation mechanism than photoionization. We exclude two objects having significant $[\text{Ne III}]\lambda 3869$ lines, and obtain 4175 ETGs.

Griffith et al. (2019) introduced a diagnostic diagram of $[O\text{ I}]\lambda 6300/H\alpha$ versus $[O\text{ III}]\lambda 5007/H\beta$ to exclude an ionization mechanism, which is excited by single-degenerate (SD) SNe Ia progenitors (Woods & Gilfanov 2014). In this model, Woods & Gilfanov (2014) employed diagnostic tools, utilizing $[O\text{ I}]$, $[\text{N I}]$ emission lines increasingly ionized by high temperatures, to test if WD progenitors could be a dominant ionization source. In Figure 2, we show our sample on the diagnostic diagram of $[O\text{ I}]\lambda 6300/H\alpha$ versus $[O\text{ III}]\lambda 5007/H\beta$, obtaining 4097 ETGs.

Figure 3 presents the relation between $W2-W3$ and $W1-W2$ colors for composite ETGs. The optimal division line (red dashed line), $W2-W3 = 2.5$, is used as the best demarcation between galaxies with and without SF (Herpich et al. 2016). Stern et al. (2012) proposed that $W1-W2 > 0.8$ of Figure 2 be the mid-IR standard by which to choose AGNs, and these measurements reveal that nuclear activity provides almost all the IR emission (Caccianiga et al. 2015). The “AGN wedge” proposed by Mateos et al. (2012) is displayed by the green lines in Figure 2.

In Figure 3, the black dots at the left of the red dashed line $W2-W3 = 2.5$ show 1845 composite ETGs without SF. The red “*” signs in Figure 3 represent those ETGs with metallicity measurements from Athey & Bregman (2009), Annibaldi et al. (2010), Bresolin (2013), and Griffith et al. (2019). One of the galaxies at the right of the red dashed line of Figure 3 is NGC 4694, which appears in the SF region of the BPT diagram of Figure 4 of Griffith et al. (2019). This galaxy should be an SF ETG. The purple triangles located in the “AGN” wedge (green solid lines) proposed by Mateos et al. (2012) are used to display ETGs with nuclear activities; here there are 24 such ETGs. The cyan diamonds, which lie to the right of the red dashed line of Figure 3, are thought to be composite ETGs with

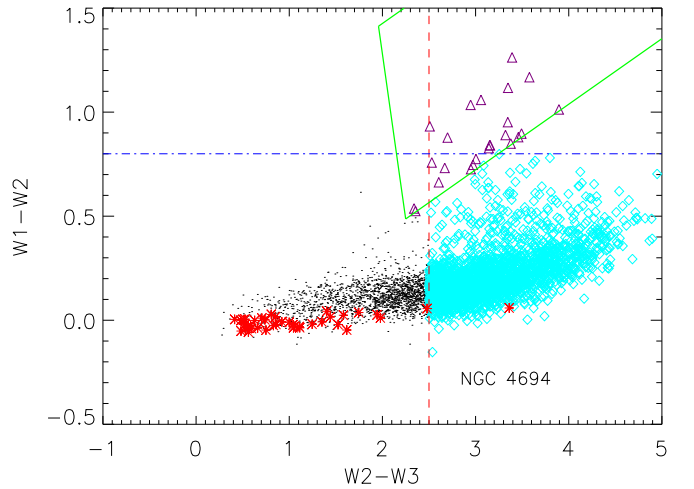


Figure 3. $W2-W3$ vs. $W1-W2$ color-color diagram for composite ETGs. The blue horizontal dotted-dashed line represents the mid-IR criterion to select AGNs proposed by Stern et al. (2012). The green solid lines display the “AGN” wedge as suggested by Mateos et al. (2012). The red vertical dashed line describes the best boundary between retired galaxies and ongoing SF galaxies. The black dots and purple triangles are composite ETGs, and the former ones have no SF or AGNs, while the latter ones exhibit AGN activities. The cyan diamonds are our study sample of ETGs with SF. The red “*” signs are those ETGs with metallicity measurements from Bregman (2009), Annibaldi et al. (2010), Bresolin (2013), and Griffith et al. (2019).

SF, because Herpich et al. (2016) found that galaxies with mid-IR color $W2-W3 > 2.5$ denote objects with SF. Less than half of all composite ETGs have SF, and we suggest that SF is a dominant excitation source in these ETGs. Finally, we derive our sample of 2218 ETGs.

3.2. Properties of These ETGs

In Figure 1, we use the BPT diagnostic diagram to show the ETG samples. The blue dotted curve represents the Kauffmann et al. (2003) semi-empirical lower boundary for SFGs, while the green dashed curve on this diagram shows the theoretical “extreme starburst line” obtained by Kewley et al. (2001) as an upper boundary for SFGs. The black and red dots present initial composite ETGs; the red dots display our final ETG sample with metallicity measurements. From Figure 1, we can see that most of the red dots are close to the blue dotted curve, and a majority of the black dots are close to the green dashed curve. This indicates that the ETGs represented by red dots may be dominated by SF.

Due to the limited sample size of ETGs, we were previously unable to completely present their MZ relations. Here, we have a chance to present it using a large ETG sample. Figure 4 shows the MZ relation for our composite ETGs with the six metallicity calibrators. We find that the range of most galaxy stellar masses is from $\log(M_*/M_\odot) \sim 10.0$ to $\log(M_*/M_\odot) \sim 11.0$. We find that these MZ relations calibrated by the six metallicity indicators do not show clearly positive correlations, and that most ETGs lie below the green fit curves in Figure 4. Next we discuss the properties of the MZ relation in the following two cases: the MZ relation of ETGs that lie below and above the median MZ relation of SFGs.

In Figures 4(a), (c), (d), and (f), the MZ relations for ETGs lie below the median MZ relations for SFGs. They employ, respectively, the metallicity indicators of R23, O32, O3N2, and O3S2 to calibrate the ETG metallicities. In Figure 4(a), the green dotted-dashed line describes a polynomial fit of data

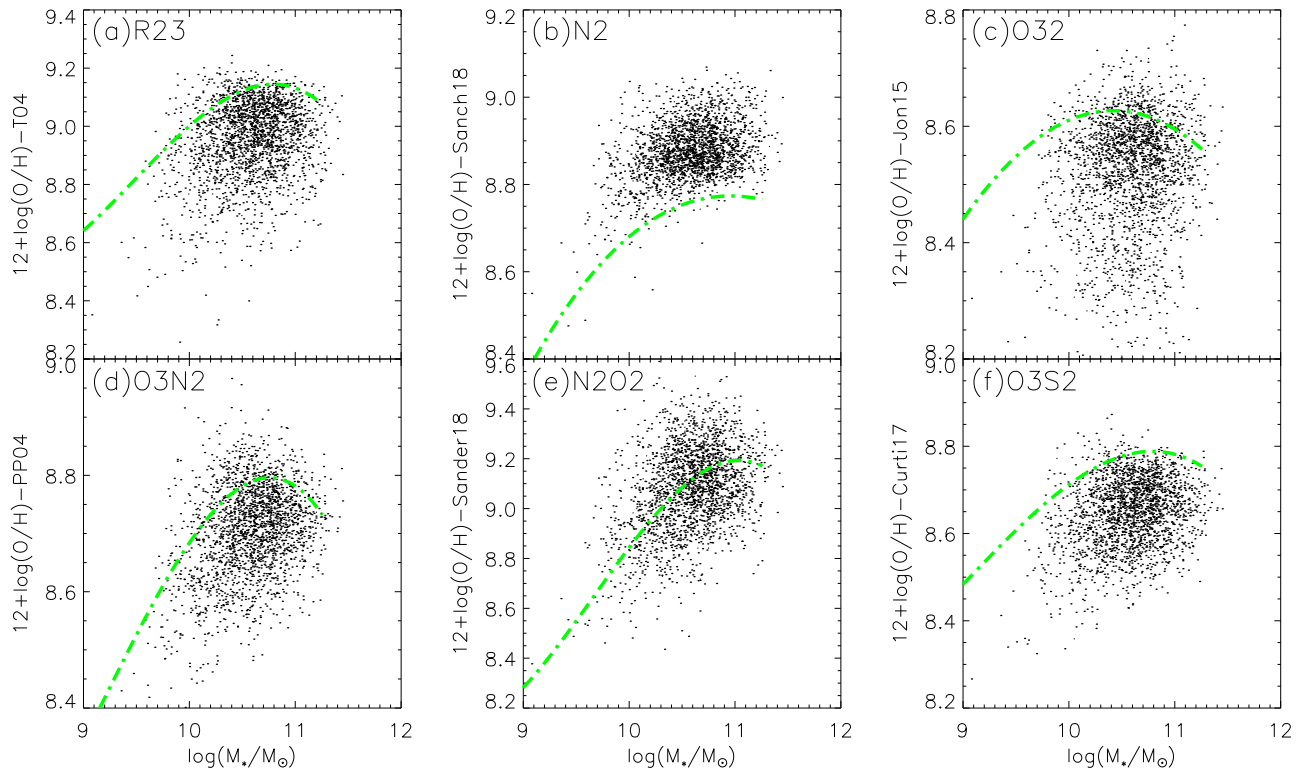


Figure 4. Comparison of the MZ relations of composite ETGs for different metallicity calibrators. The green dotted–dashed lines represent a polynomial fit of data from 93,089 SFGs (see the text).

(deriving 93,089 SFGs from the MPA–JHU catalog for the SDSS DR7 with the same sample selection method of Wu et al. 2019, except $S/N > 2$ for $[\text{O II}]\lambda\lambda 3227, 3229$, and $[\text{N II}]\lambda 6584$), which have median values of 30 bins, 0.1 dex in mass, and include more than 100 galaxies. The MZ relation does not clearly show a positive correlation, with the Spearman coefficient $r = 0.17$. Also, the MZ relations calibrated by metallicity indicators of Jon15, PP04, and Curti17 do not present a positive correlation, with the Spearman coefficient $r = 0.1$, $r = 0.26$, and 0.21 , respectively. We can see that most of the composite ETGs displayed in Figure 4(a) lie below the green fit line at a given stellar mass. Figures 4(c), (d), and (f) also show the same result, with a majority of ETGs lying below the median MZ relation of SFGs. The middle panel of Figure 9 of Griffith et al. (2019) shows the MZ relation of ETGs using the O3N2 metallicity calibration of Pettini & Pagel (2004). We can see that most ETGs may be below the MZ relation of SFGs. Combining the results of our MZ relation and that of Griffith et al. (2019), we find that the MZ relation of these ETGs may be different from that of late-type galaxies; this indicates that the metallicities of ETGs are likely to be lower than those of late-type galaxies at a fixed stellar mass.

Figures 4(b) and (e) do not show a significantly positive correlation, with the Spearman coefficient $r = 0.28$ and $r = 0.31$, respectively. In these two figures we find that the metallicity calibrators of Sánchez18 and S and Sander18 do not show the result of Figures 4(a), (c), (d), and (f); in addition, almost all of the ETGs lying above the green fit line adopt the N2 metallicity indicator. In Figure 4(b), The Sánchez18 calibrator employs the N2 indicator ($[\text{N II}]\lambda 6584/\text{H}\alpha$) and Equation (3) of Sánchez-Almeida et al. (2018). Their metallicity increases with increasing N2. Similarly, in Figure 4(e), we find that about 52% of ETGs lie below the green fit curve. We suggest that this

may originate from the metallicity calibrator of S and Sander18, and the metallicity increases with increasing indicator N2O2 ($[\text{N II}]\lambda 6584/([\text{O II}]\lambda\lambda 3727, 3729)$). In the top panel of Figure 9 of Griffith et al. (2019), we find that most ETGs from Athey & Bregman (2009), Annibali et al. (2010), and Griffith et al. (2019) have higher metallicity, by about 0.2 dex, than SFGs in O3N2 metallicity calibrated from the PP04–N2 metallicity indicator. In the bottom panel, we also find that these ETGs have higher about 0.1 dex in metallicity than SFGs using PP04–O3N2 indicator calibrated from the KD02–N2O2 estimator. We find that their results are almost consistent with our results shown in Figures 4(b) and 4(d). According to the Coziol et al. (1999) model, the nitrogen production occurs almost ceaselessly in SFGs, but the oxygen enrichment is only produced in massive star evolution, and the two productions proceed alternately (Wu & Zhang 2013). It is difficult to observe oxygen production in ETGs, while nitrogen production is easier to observe because ETGs tend to experience low-level SF (Yi et al. 2005; Kaviraj et al. 2007). Therefore, we suggest that these metallicity calibrators, wherein metallicity increases with N-enrichment (for example, the Sánchez18 and S and Sander18 metallicity indicators), can be used to successfully calibrate metallicities for SFGs, but may not be able to estimate the metallicities of ETGs.

In Figure 5, we show the distribution of D_n4000 for our final ETG sample. We find that the majority of ETGs with metallicity measurements have younger stellar populations, and about 85% of these ETGs display $D_n4000 < 1.6$. These ETGs with $W2-W3 > 2.5$ clearly show SF (Herpich et al. 2016) and approach the Kauffmann et al. (2003) semi-empirical line; therefore, most of them should have younger stellar populations.

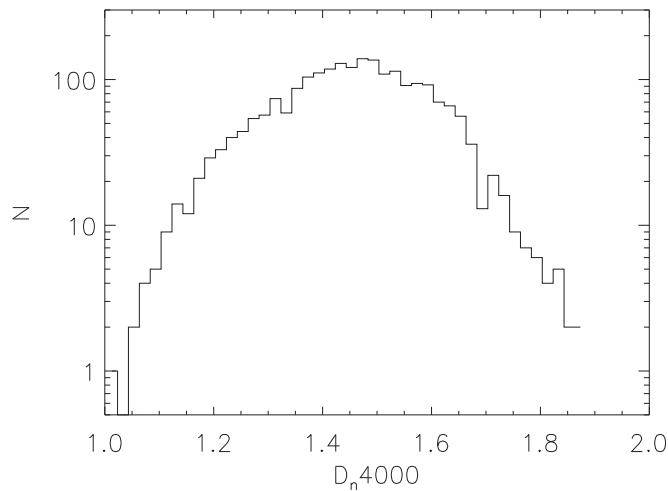


Figure 5. Distribution of D_n4000 for our ETG sample with metallicity measurements.

4. Summary

In this Letter we derive the observational data of 6048 ETGs, and cross-match Galaxy Zoo 1 data with SDSS DR7 MPA-JHU emission-line measurements. We exclude various ionization sources to explore the metallicity measurement of ETGs, and investigate the properties of these ETGs. We summarize our main results as follows.

1. We utilize the optimal division line of $W2-W3 = 2.5$ as the diagnostic tool, which selects ETGs ($W2-W3 > 2.5$) with SF as our composite ETG sample. We obtain the final sample of 2218 ETGs, and can calculate their metallicities.

2. We find that our ETGs tend to be located close to the semi-empirical lower limit for SFGs proposed by Kauffmann et al. (2003) in the BPT diagram. Moreover, we find that these ETGs have younger stellar populations, and 85% of the ETGs have $D_n4000 < 1.6$.

3. The MZ relation for ETGs is shown, and we find that the metallicity of these ETGs tends to be lower than SFGs at the same galaxy stellar mass. We use five metallicity calibrators to check the result. We find that three of these metallicity calibrators (R23, O32, and O3S2) can give consistent results, while the N2O2 and N2 calibrators do not obtain the same result. We suggest that these metallicity calibrators, wherein metallicity increases with N-enrichment (for instance, the Sanch18 and S and Sander18 metallicity calibrators), can be used to successfully calibrate metallicities for SFGs, but may not be able to estimate the metallicities of ETGs.

Y.Z. Wu thanks the anonymous referee for valuable suggestions and comments that improved the quality of this Letter. This work was supported by the Natural Science Foundation of China (NSFC; No. 11703044).

References

- Abazajian, K. N., Adelman-McCarthy, J. K., Agüeros, M. A., et al. 2009, *ApJS*, **182**, 543
- Allen, M. G., Groves, B. A., Dopita, M. A., Sutherland, R. S., & Kewley, L. J. 2008, *ApJS*, **178**, 20
- Andrews, B. H., & Martini, P. 2013, *ApJ*, **765**, 140
- Annibali, A., Bressan, A., Rampazzo, R., et al. 2010, *A&A*, **519**, A40
- Athey, A. E., & Bregman, J. N. 2009, *ApJ*, **696**, 681
- Baldwin, J. A., Phillips, M. M., & Terlevich, R. 1981, *PASP*, **93**, 5
- Belfiore, F., Maiolino, R., Maraston, C., et al. 2016, *MNRAS*, **461**, 3111
- Blanton, M. R., Schlegel, D. J., Strauss, M. A., et al. 2005, *AJ*, **129**, 2562
- Bresolin, F. 2013, *ApJL*, **772**, L23
- Brown, J. S., Martini, P., & Andrews, B. H. 2016, *MNRAS*, **458**, 1529
- Caccianiga, A., Antón, S., Ballo, L., et al. 2015, *MNRAS*, **451**, 1795
- Chabrier, G. 2003, *PASP*, **115**, 763
- Combes, F., Young, L. M., & Bureau, M. 2007, *MNRAS*, **377**, 1795
- Coziol, R., Reyes, R. E. C., Considère, S., Davoust, E., & Contini, T. 1999, *A&A*, **345**, 733
- Curti, M., Cresci, G., Mannucci, F., et al. 2017, *MNRAS*, **465**, 1384
- Davis, T. A., Rowlands, K., Allison, J. R., et al. 2015, *MNRAS*, **449**, 3503
- Finkelman, I., Moiseev, A., Brosch, N., & Katkov, I. 2011, *MNRAS*, **418**, 1834
- Geréb, K., Catinella, B., Cortese, L., et al. 2016, *MNRAS*, **462**, 382
- Goudfrooij, P., & de Jong, T. 1995, *A&A*, **298**, 784
- Goudfrooij, P., de Jong, T., Hansen, L., & Norgaard-Nielsen, H. U. 1994, *MNRAS*, **271**, 833
- Griffith, E., Martini, P., & Conroy, C. 2019, *MNRAS*, **484**, 562
- Herpich, F., Mateus, A., Stasińska, G., Cid Fernandes, R., & Vale Asari, N. 2016, *MNRAS*, **462**, 1826
- Herpich, F., Stasińska, G., Mateus, A., Vale Asari, N., & Cid Fernandes, R. 2018, *MNRAS*, **481**, 1774
- Jones, T., Martin, C., & Cooper, M. C. 2015, *ApJ*, **813**, 126
- Kauffmann, G., Heckman, T. M., Tremonti, C., et al. 2003, *MNRAS*, **346**, 1055
- Kaviraj, S., Peirani, S., Khochfar, S., Silk, J., & Kay, S. 2009, *MNRAS*, **394**, 1713
- Kaviraj, S., Schawinski, K., Devriendt, J. E. G., et al. 2007, *ApJS*, **173**, 619
- Kewley, L. J., Dopita, M. A., Sutherland, R. S., Heisler, C. A., & Trevena, J. 2001, *ApJ*, **556**, 121
- Kewley, L. J., Groves, B., Kauffmann, G., & Heckman, T. 2006, *MNRAS*, **372**, 961
- Kewley, L. J., Jansen, R. A., & Geller, M. J. 2005, *PASP*, **117**, 227
- Kroupa, P. 2001, *MNRAS*, **322**, 231
- Krumm, N., & Salpeter, E. E. 1979, *ApJ*, **228**, 64
- Kumari, S., Maiolino, R., Belfiore, F., & Curti, M. 2019, *MNRAS*, **485**, 367
- Lagos, C. P., Davis, T. A., Lacey, C. G., et al. 2014, *MNRAS*, **443**, 1002
- Lintott, C. J., Schawinski, K., Bamford, S., et al. 2011, *MNRAS*, **410**, 166
- Lintott, C. J., Schawinski, K., Slosar, A., et al. 2008, *MNRAS*, **389**, 1179
- Mateos, S., Alonso-Herreor, A., Carrera, F. J., et al. 2012, *MNRAS*, **426**, 3271
- Oosterloo, T., Morganti, T., Crocker, A., et al. 2010, *MNRAS*, **409**, 500
- Pettini, M., & Pagel, B. E. J. 2004, *MNRAS*, **348**, 59
- Sánchez-Almeida, J., Caon, N., Muñoz-Tuñón, C., Filho, M., & Cerviño, M. 2018, *MNRAS*, **476**, 4765
- Sanders, R. L., Shapley, A. E., Kriek, M., et al. 2018, *ApJ*, **858**, 99
- Sarzi, M., Alatalo, K., Blitz, L., et al. 2013, *MNRAS*, **432**, 1845
- Serra, P., Oosterloo, T., Morganti, R., et al. 2012, *MNRAS*, **422**, 1835
- Sparks, W. B., Macchetto, F., & Golombek, D. 1989, *ApJ*, **345**, 153
- Stern, D., Assef, R. J., Benford, D. J., et al. 2012, *ApJ*, **753**, 30
- Thilker, D. A., Bianchi, L., Schiminovich, D., et al. 2010, *ApJL*, **714**, L171
- Tremonti, C. A., Heckman, T. M., Kauffmann, G., et al. 2004, *ApJ*, **613**, 898
- Woods, T. E., & Gilfanov, M. 2014, *MNRAS*, **439**, 2351
- Wright, E. L., Eisenhardt, P. R. M., Mainzer, A. K., et al. 2010, *AJ*, **140**, 1868
- Wu, Y.-Z., & Zhang, S.-N. 2013, *MNRAS*, **436**, 934
- Wu, Y.-Z., Zhang, W., & Zhao, Y.-H. 2019, *MNRAS*, **486**, 5310
- Yi, S. K., Yoon, S.-J., Kaviraj, S., et al. 2005, *ApJL*, **619**, L111
- Zhang, K., Yan, R.-B., Bundy, K., et al. 2017, *MNRAS*, **466**, 3217